

Structural/phase changes and enhanced interlayer interactions in Ni-doped MoS₂ from density functional theory

Rijan Karkee, Enrique Guerrero, and David A. Strubbe*

Department of Physics, University of California, Merced, Merced, CA 95343

E-mail: dstrubbe@ucmerced.edu

Abstract

The crystal structure of MoS₂ with strong covalent bonds in plane and weak Van der Waals interactions out of plane gives rise to interesting properties for applications such as optoelectronics, solid lubrication, and catalysis, which can be enhanced by transition-metal doping. However, the mechanisms for improvement and even the structure of the doped material can be unclear, which we address in this paper with theoretical calculations. Building on our previous work on Ni-doping of the 2H phase, now we explore polytypes (1H and 1T monolayers, and 3R bulk), to determine favorable sites for Ni and the doping effect on crystal structure, electronic properties and the layer dissociation energy. We find the most favorable intercalation/adatom sites are tetrahedral intercalation for 3R (like 2H), Mo-atop for 1H, and hollow site for 1T. The relative energies indicate a possibility of phase change from 2H to 3R with substitution of Mo or S. We find metallic behavior in Mo-substituted 3R and 2H, and in-gap states for Mo- and S-substituted 1H, which could have interesting optoelectronic applications. Doping the 1T phase resulted in reconstructions leading to a metal-semiconductor transition. We find a large enhancement in the interlayer interactions of Ni-doped

MoS₂, opposite to the effect of other transition metals. For lubrication applications, this increased layer dissociation energy could be the mechanism of low wear. Our systematic study shows the effect of doping concentration and is extrapolated to the low-doping limit. This work gives insight into the previously unclear structure of Ni-doped MoS₂ and how it can be detected experimentally, the relation of energy and structures of doped monolayers and bulk systems, the electronic properties under doping, and the effect of doping on interlayer interactions.

1 Introduction

There has been great interest in transition metal dichalcogenides, particularly in MoS₂ which has been used in a wide variety of applications because of its unique physical, optical and electrical properties.¹⁻³ The tunability of band gap from direct to indirect,^{1,2} good electron mobility,⁴ the possibility of defect engineering including creating quantum emitters,⁵ and high current-carrying capabilities⁶ open great potential in optics and electronics. MoS₂ has already shown promising applications in lubrication, hydrodesulfurization, and optoelectronics.⁷⁻¹⁰ Theoretical and experimental work has shown that transition-metal-doping in MoS₂ can improve catalytic reactivity,¹¹⁻¹³ lubrication¹⁴ and gas sensing.^{15,16} However, the detailed mechanism is still unclear for improved catalysis and lubrication with doping, and in general the exact location of dopants in MoS₂ is also uncertain. Our previous work addressed the most favorable sites for Ni in 2H-MoS₂ as a function of chemical potential.¹⁷ We now extend this to a systematic exploration of different polytypes and careful consideration of doping concentration-dependence. This study will look specifically at implications for solid lubrication, but also give insight into optoelectronic and other fundamental properties.

MoS₂ is a layered structure with weak Van der Waals forces between layers and strong covalent forces within the layers giving rise to interesting applications in solid lubricants because the weakly bound layers can slide against each other easily. Graphite is a commonly used solid lubricant, which also has a layered Van der Waals structure, but it needs to adsorb

oxygen and moisture to develop the low shear strength necessary for lubrication.¹⁸ MoS₂, on the other hand, works well under vacuum but shows degradation in lubrication under humidity and high temperature, for unclear reasons.¹⁹ Therefore MoS₂ is preferred for solid lubrication in space applications such as NASA’s James Webb Space Telescope¹⁰ where the wide range of temperatures precludes the use of oils or greases for lubrication of moving parts.

A clear understanding of the mechanisms by which Ni-doped MoS₂ enhances lubrication performance of pristine MoS₂ is still lacking. A recent review²⁰ discusses low friction mechanisms based on ordering of crystallites in adjacent platelets. The early experimental work of Stupp²¹ studied the friction properties in MoS₂ doped with various transition metals. MoS₂ doped with Ni or Ta showed the best results in terms of stable friction, excellent endurance, easy control, good effect on aging, and lower coefficient of friction than pristine MoS₂. Later, other researchers also confirmed the lower coefficient of friction for Ni-doping.²² Ni is more abundant and less expensive than Ta,^{23,24} making it more attractive. There are already some studies on Ni-doped MoS₂ monolayers and nanosheets, for catalysis in solar hydrogen production,¹³ adsorption of CO or NO for potential gas sensors,¹⁵ or adsorption of O₂ molecules,²⁵ but tribological applications were not considered. Therefore there is a clear need for theoretical and atomistic study of Ni-doped MoS₂ as a lubricant.

Most of the literature on doped MoS₂ is focused on electronic, optical, and catalytic applications and there have been only a small number on tribology. Different dopants such as Ni, Cr, Ti, Au, Zr and Sb₂O₃ have been studied for the improvement of tribological properties.²⁶ One popular proposed mechanism is increase in hardness as a result of distortion of the MoS₂ crystal structure, and the resultant hardness reduces wear which is crucial to coating life (endurance).^{27,28} A recent experiment specifically on Ni showed that wear is reduced by doping, extending the lifetime of MoS₂ films.²⁹ Driven by those experimental results, we investigated Ni-doped MoS₂ structures and properties theoretically by Density Functional Theory (DFT). MoS₂ can exist in different phases:²⁶ 2H and 3R bulk, and 1T and

1H monolayers. Friction in MoS₂ involves sliding of layers, and 2H and 3R phases only differ by stacking, *i.e.* sliding followed by rotation. While 2H is the most studied bulk polytype and the predominant naturally occurring one, 3R is also found naturally and has a very similar energy to 2H.²⁶ Also, it is found that doping may alter the phase: for example, Li intercalation in MoS₂ causes a change from 2H to 1T phase³⁰ and Nb substitution on Mo favors 3R over 2H.³¹ The possibility of alteration in phase due to doping, layer sliding, or the effect of mechanical load in tribology application is a motivation for considering other phases in MoS₂, as well as to assess whether deliberate production of different polytypes could improve performance.

In this paper, we will consider the effect of Ni-doping in MoS₂ polytypes, and investigate changes in local structure, the energetics of dopants at different sites, the possibility of phase changes, and the effect on interlayer interactions. Section 2 discusses the choice of dopant structures of different polytypes in MoS₂. Section 3 presents results on: (a) doping formation energy, (b) effect of doping on crystal structure and local structure, (c) effect on electronic properties (including oxidation states) and (d) effect on the layer dissociation energy. Finally, Section 4 concludes to discuss the impact of Ni-doping, experimentally measurable signatures of different doped structures, and a possible explanation for low wear in MoS₂ lubrication.

2 Structure and doping site selection

MoS₂ can exist in different possible structures in bulk and monolayer phases (Fig. 1).²⁶ The known phases of MoS₂ are 1H (hexagonal monolayer), 1T (trigonal monolayer), 2H (hexagonal bulk) and 3R (rhombohedral bulk), all semiconducting except for 1T. The 1H, 2H and 3R phases contain 3, 6, and 9 atoms in a conventional unit cell respectively, and they differ by stacking. In 1H and 1T, each sheet of MoS₂ is stacked exactly above each other (AA stacking). In 2H, the Mo atom in one layer is above an S atom of the preceding one, forming AB stacking, and 3R has ABC stacking with 3 sheets per conventional unit cell. 1H and

1T differ by coordination around Mo where 1H has trigonal prismatic coordination and 1T has octahedral bonding. Theoretical^{32,33} calculations and experiments³⁴ show 1T is unstable with respect to distortions and forms more stable phases such as 1T', 1T'' or 1T'''.³⁵ 1T' has been calculated to be a topological insulator.³⁶ In 3R, all sheets have the same orientation, but 2H has inversion symmetry between sheets. Our DFT calculation (Fig. 2) shows only a small difference in total energy of the 2H and 3R phases (2H is lower by 1.2×10^{-4} eV per MoS_2 unit). In the monolayers, we found 1H phase is more favorable than 1T by 0.85 eV per MoS_2 unit. Both these results agree with previous literature.³⁷

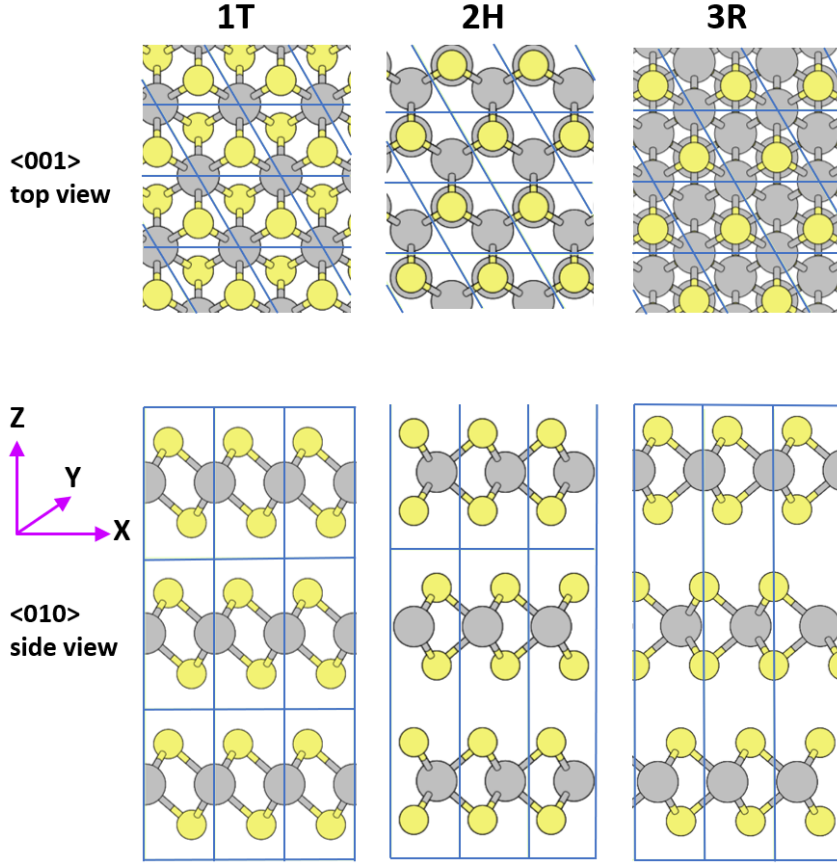


Figure 1: Structure of MoS_2 polytypes with conventional unit cell marked by blue lines. Mo is gray and S is yellow. 1H is a single monolayer sheet of MoS_2 containing 3 atoms per unit cell, as in each sheet of 2H or 3R.

The most probable sites for dopants¹⁷ in MoS_2 include substitutions and intercalations for bulk or adatoms for monolayers, and are shown in Fig. 3. We have also considered

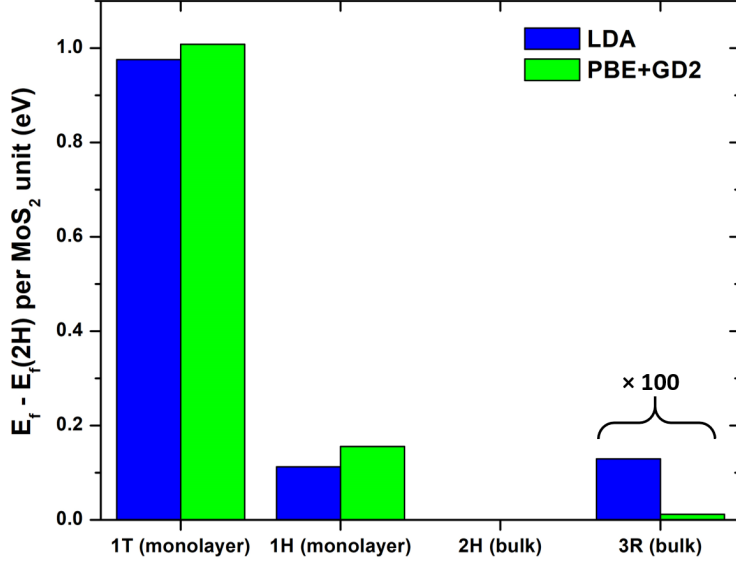


Figure 2: DFT calculation of formation energy per unit of MoS_2 in MoS_2 polytypes, with respect to 2H- MoS_2 . The most stable monolayer is 1H phase, and bulk 2H and 3R are almost equally stable. The formation energy with respect to bulk Mo and S for 2H is -2.59 eV with PBE+GD2 and -3.05 eV with LDA.

the bridge site along the Mo-S bond but found that intercalation/adatom in this site was unstable and relaxed to tetrahedral intercalation in 2H and 3R, Mo-atop in 1H and hollow site in 1T. Therefore the bridge site was not considered in further calculations. We will use these sites to study the various structural and electronic properties of Ni-doped MoS_2 .

3 Results and discussion

3.1 Doping Formation Energy

The doping formation energy tells us the energy needed to incorporate the dopant (Ni) into the host system (MoS_2). As noted in our previous work,¹⁷ the doping formation energy depends on the chemical potentials during the growth process, and so the relative favorability between different stoichiometries (*e.g.* substitution *vs.* intercalation) depends on the

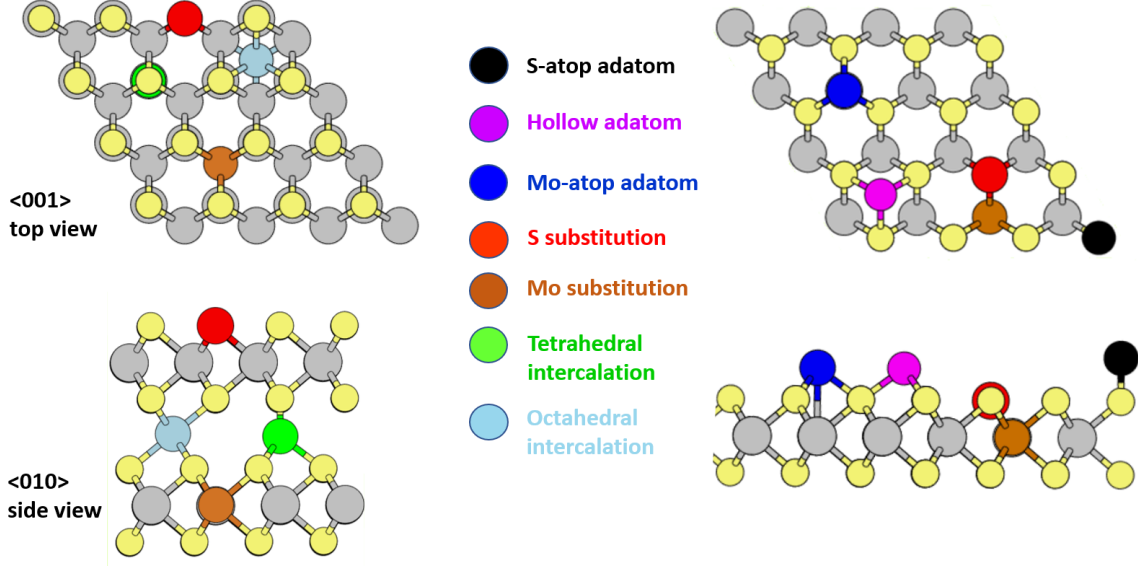


Figure 3: Different dopant sites for Ni in 2H (left) and 1H (right) MoS₂ with top view (upper) and side view (lower). Sites include substitution in the Mo site or S site, tetrahedral or octahedral intercalation for bulk phases (2H and 3R), and Mo-atop, S-atop and hollow adatoms for 1H and 1T (monolayers). 3R sites are similar to 2H (see detail in Fig. 6). The top layer is the same for 1H and 1T.

conditions. The doping formation energy is calculated as:

$$E_{\text{formation}} = E_{\text{system}} - NE_{\text{pristine}} - \mu_{\text{Ni}} + \mu_{\text{removed}} \quad (1)$$

for substitution cases, and

$$E_{\text{formation}} = E_{\text{system}} - NE_{\text{pristine}} - \mu_{\text{Ni}} \quad (2)$$

for intercalation cases, where E_{system} is the energy of the doped system, N is the multiplicative factor for supercell size (for example, $N=12$ for $2 \times 2 \times 3$ supercell), E_{pristine} is the energy per unit cell of the corresponding phase of MoS₂, and μ_{Ni} and μ_{removed} are the chemical potential of the dopant (Ni) and removed atom, respectively. We consider μ_{Ni} equal to the energy per atom of bulk Ni (“Ni-rich” conditions). For substitution cases, we consider equilibrium conditions for the given phase where $\mu_{\text{Mo}} + 2\mu_{\text{S}} = E_{\text{pristine}}/N_{\text{f.u.}}$ and $N_{\text{f.u.}}$ is the number of

MoS₂ units per pristine cell; then we look at conditions where either $\mu_{\text{Mo}} = E_{\text{Mo}}$ (“Mo-rich,” which favors S substitution) or $\mu_{\text{S}} = E_{\text{S}}$ (“S-rich”, which favors Mo substitution). These energies of Mo and S are calculated from their bulk phases, as in previous literature.^{17,38,39} For example, in $2 \times 2 \times 1$ Mo substitution by Ni in 2H, E_{system} is the energy of NiMo₇S₁₆, N is 4, E_{Ni} and E_{removed} are the energy per atom of bulk Ni and Mo and E_{pristine} is energy of Mo₂S₄. Similarly in $4 \times 4 \times 1$ Ni intercalation in 2H, E_{system} is the energy of NiMo₃₂S₆₄ and N is 16.

3.1.1 Monolayers

The doping formation energies for Ni-doped MoS₂ in 1H and 1T phases with Mo or S substitution and different adatom sites (Fig. 3) were computed with supercells from $2 \times 2 \times 1$ to $4 \times 4 \times 1$. Fig. 4 shows results for adatoms in $4 \times 4 \times 1$ supercell. We find doping formation energy is lower in 1T than 1H, which means Ni is easier to dope into 1T phase. In 1H, the adatom on Mo is the energetically favored adatom site and this result – along with Mo-Ni (2.52 Å) and Ni-S (2.12 Å) bond lengths – is in accordance with previous literature.⁴⁰ In 1T, hollow is the most favored adatom site and similar results were previously reported.⁴¹

Doping formation energy for substitution of Mo or S is also lower in 1T than 1H. Fig. 5(a) shows the substitutional doping formation energy in monolayer MoS₂. At low doping concentration, we found negative doping formation energy for 1T substitution, except for S substitution in S-rich conditions, and hence Ni can be incorporated favorably into 1T-MoS₂. A recent experiment³⁴ reported synthesis of 1T with Ni substituting for Mo in accordance with this result. Under S-rich conditions, Mo substitution is always favorable. Under Mo-rich conditions, negative doping formation energy in Mo substitution was seen starting from the $3 \times 3 \times 1$ supercell (below 4% atomic concentration), whereas high doping had a positive doping formation energy.

Despite the lower doping formation energies for 1T, the total energy of Ni-doped 1H is lower than Ni-doped 1T for each doping cases, as shown in Fig. 5(b). This means that

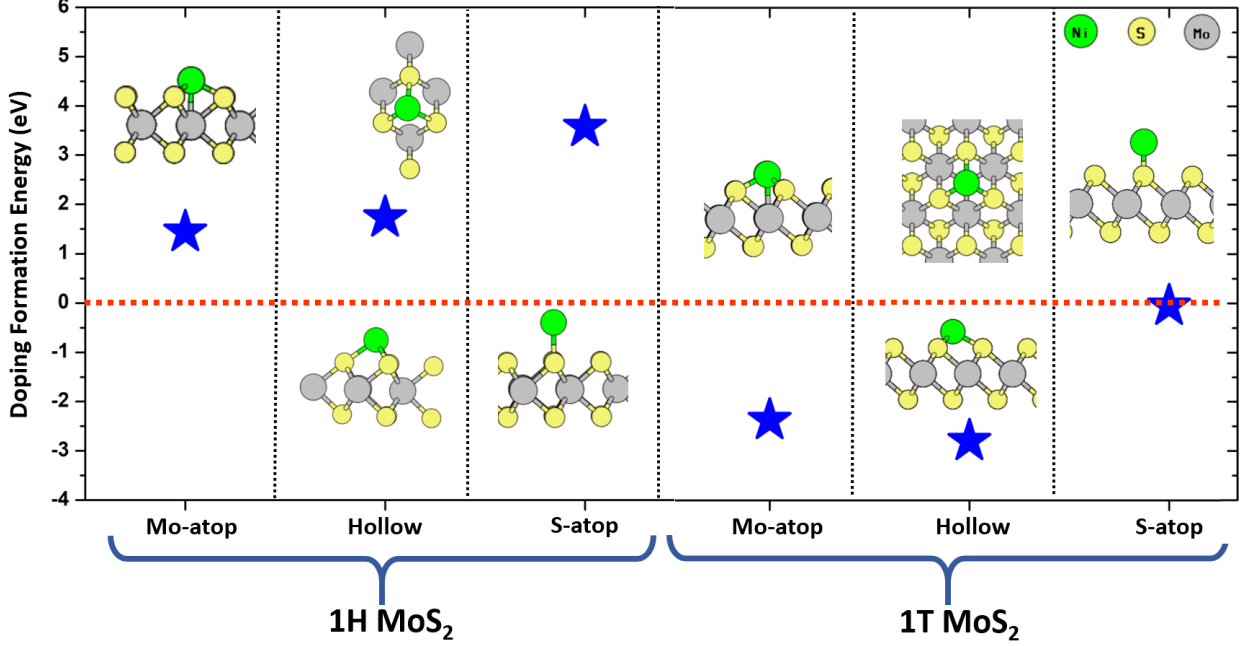


Figure 4: The doping formation energy for various adatom sites in a $4 \times 4 \times 1$ supercell of monolayer 1H and 1T. The doping formation energy is calculated with reference to bulk Ni and pristine 1H- or 1T-MoS₂. The star indicates doping formation energy and the images depict the structure (side or top view).

given Mo, S and Ni atoms, formation of Ni-doped 1H is more favorable than Ni-doped 1T. Ni-doping does reduce the difference in energy between 1H and 1T, which is partly due to reconstruction of the doped 1T (Section 3.2). Mo substitution showed the largest reduction in the energy difference. The difference becomes smaller with high doping concentration, when the impact of Ni is proportionately greater. For example, in Mo substitution, the difference is 0.23 eV and 0.42 eV per MoS₂ unit in 8% and 2% of doping concentration respectively. A phase transition from Ni-doped 1H to 1T might be possible at elevated temperature at higher doping concentration, particularly for the Mo-substituted case.

3.1.2 Bulk

The energetics of Ni-doped MoS₂ in bulk phases (2H and 3R) are presented here. In 2H, tetrahedral intercalation is more energetically favored than octahedral intercalation at all concentrations. The tetrahedral intercalation site is Mo-atop and S-atop with respect to the

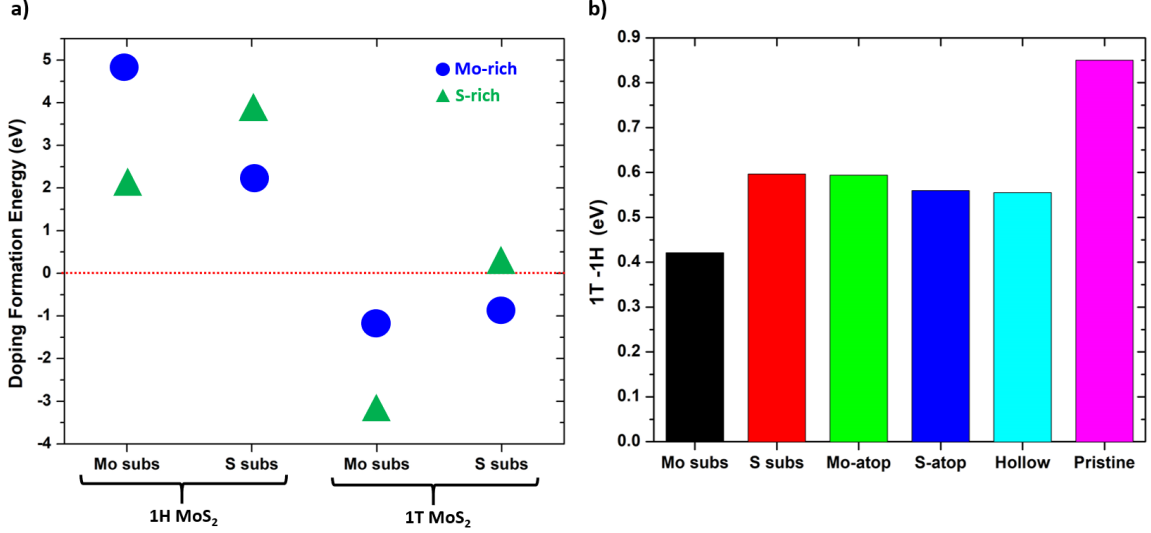


Figure 5: (a) Doping formation energy for Mo and S substitution in 1H and 1T phases, with reference to bulk Ni and pristine 1H or 1T MoS₂, and chemical potentials of Mo and S at Mo-rich or S-rich conditions. Negative doping formation energy for Mo-substituted 1T indicates this doping is energetically favorable, and more favorable than in 1H. (b) Energy difference (1T-1H) per MoS₂ for doped and undoped monolayers with $4 \times 4 \times 1$ supercell. The lower total energy for 1H indicates formation of 1H phase is more likely given isolated Mo, Ni and S atoms.

sheets on the either side as shown in Fig. 6, whereas octahedral intercalation consists of hollow sites on each sheet. In 3R, we find three metastable intercalation cases. There are two sites with tetrahedral geometry: in one, the Ni atom is Mo-atop for one sheet and S atop for the other (“Mo/S-atop”); in the second, the Ni atom is at the hollow site for one sheet and Mo-atop for the other (“hollow/Mo-atop”). The third intercalation site has trigonal pyramidal geometry and is Mo-atop for one sheet and bridge site for the other. Octahedral intercalation is not possible in 3R. In 3R, the Mo/S-atop tetrahedral intercalation (similar to 2H tetrahedral intercalation) is the most favored intercalation site, by around 0.5 eV (Table S5). These most favorable sites in bulk phases are clearly related to energetics in the 1H phase. As discussed in Section 3.1.1, adatom on Mo is the most favorable site in 1H and all the most favored sites in bulk (2H and 3R) involve Mo-atop. The intercalant acts as an adatom for the neighboring layers and lower doping formation energy is achieved if the intercalant site resembles the monolayers’ lowest-energy adatom sites.

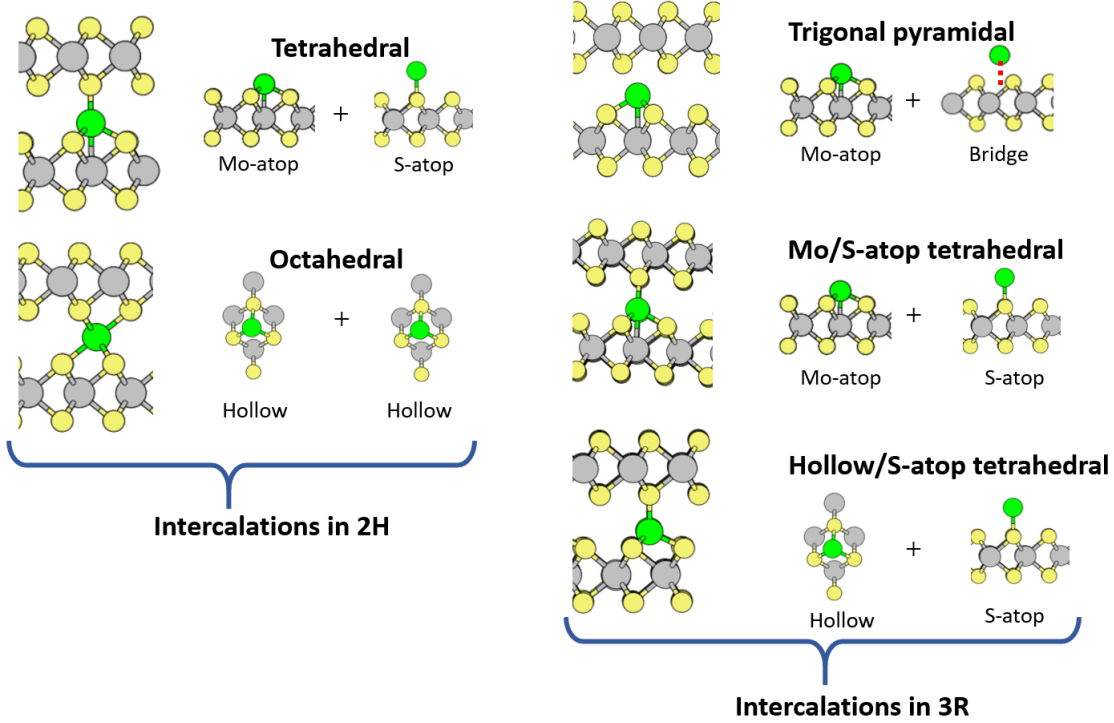


Figure 6: Intercalations in 2H and 3R classified by bonding geometry. The pair of images next to each bulk structure shows the site with respect to the 1H monolayers on each side. Tetrahedral for 2H, and Mo/S-atop tetrahedral for 3R, are the most favorable.

3.1.3 Concentration Dependence of Doping Formation Energy

We can extrapolate defect energies to the low concentration limit as a function of inverse volume ($1/V$) according to the scheme of Makov and Payne (based on behavior of both local strain and electrostatics).⁴² We use this method for the doping formation energy and show results for the 2H phase in Fig. 7. The doping formation energies for each polytype and concentration are tabulated in Tables S1-S5. Variation in doping formation energy is small along the z -axis ($1 \times 1 \times N$ and $2 \times 2 \times N$) in all cases, expected due to weak interaction between layers. This finding indicates the energetics of doped bilayers are similar to bulk. The doping formation energy for in-plane supercells depends significantly on the size for small supercells ($N \times N \times 1$ and $N \times N \times 2$), but converges at high supercell size. The limit of low doping concentration can be found by extrapolation to $1/V = 0$ (red line in Fig. 7) as tabulated in Table S6. Low doping concentration calculations involve increasingly large

number of atoms and it is more efficient to extrapolate.

This supercell series scheme and extrapolation to $1/V = 0$ are useful also for understanding interactions between dopants. In 2H, S substitution doping formation energies span a range of 0.80 eV from $1 \times 1 \times 1$ to converged, tetrahedral intercalation spans 0.08 eV, octahedral spans 0.21 eV, and Mo substitution spans the largest range, 1.77 eV. The trend is similar in 3R where Mo substitution leads by 1.92 eV, followed by S substitution with 0.70 eV and then intercalations with 0.08 eV on average, as shown in Fig. S1. The energy changes with concentration are due to interaction between dopants, and so the results demonstrate that Mo substitution has the most interaction, S substitution less, and intercalations very little. The negligible Ni-Ni interaction in intercalations is also seen by the fact that doubly intercalated 2H structures (one Ni between each pair of layers) have almost the same doping formation energy as the ones with one Ni per cell (Table S3). In the monolayer, the difference in doping formation energy with increase in supercell sizes (or decrease in doping concentration) is smaller in 1H than 1T, giving faster convergence with smaller magnitude of slope vs. $1/V$ (shown in Fig. S2 and S3). The slow convergence for 1T is due to reconstruction with Ni-doping which varies due to commensurability with the supercell.

When we compared the total energy with different supercell sizes but the same number of MoS_2 units, we found a significant difference (~ 1 eV) for smaller supercells ($1 \times 1 \times 4$ vs $2 \times 2 \times 1$) but much less (~ 0.2 eV) with larger supercells ($4 \times 4 \times 1$ vs $2 \times 2 \times 4$). This variation arises from the spatial arrangement of dopant atoms and can be thought as micro-clustering of dopants or the effect of local ordering of dopants. The reduction in differences at low doping can be clearly observed in the extrapolated lines in Fig. 7 where the doping formation energies are closer for different supercells of the same volume.

Next, we compared the energy difference between doped 2H and 3R to look for the possibility of phase changes. To compare directly the energy of doped 2H and 3R structures, we designed supercells containing equal numbers of MoS_2 units: *e.g.* $2 \times 2 \times 2$ for 3R and

$2 \times 2 \times 3$ for 2H have 24 units of MoS_2 ($\sim 1\%$ Ni concentration). We also constructed supercells from the primitive cell of 3R that contains only one MoS_2 unit, therefore $1 \times 1 \times 2$ and $2 \times 2 \times 2$ have 2 ($\sim 15\%$ Ni concentration) and 8 ($\sim 4\%$ Ni concentration) MoS_2 units, which are comparable to $1 \times 1 \times 1$ and $2 \times 2 \times 1$ of 2H. Energy differences are shown in Fig. 7(d). Recall that 3R is slightly higher in energy than 2H by only $\Delta E_{3\text{R}-2\text{H}} = 1.2 \times 10^{-4}$ eV per MoS_2 . Mo-substituted 3R is lower in energy $\sim 4\Delta E_{3\text{R}-2\text{H}}$ at low doping concentration, and $\sim 200\Delta E_{3\text{R}-2\text{H}}$ at high doping concentration. S-substituted 3R is also favored over 2H by $\sim 20\Delta E_{3\text{R}-2\text{H}}$ at low concentration and $\sim 350\Delta E_{3\text{R}-2\text{H}}$ at high concentration. This suggests a possibility of phase change from 2H to 3R in substitutional doping. In experiment, Mo substitution by Ni was reported to modify the stacking sequence of MoS_2 layers forming 3R⁴³ and this is consistent with our finding of the favorability of 3R for Mo substitution. Similarly, a phase change from 2H to 3R was reported for Nb substitution of Mo in MoS_2 .³¹ By contrast, for tetrahedral intercalation, doped 2H is lower than doped 3R (Mo/S-atop) by ~ 11 and ~ 150 times $\Delta E_{3\text{R}-2\text{H}}$ at low and high concentration, respectively, further strengthening the stability of 2H over 3R.

We additionally constructed phase diagrams of the stable doping site as a function of chemical potentials μ_{Mo} and μ_{S} , for each polytype, as we did previously for 2H- MoS_2 .¹⁷ These phase diagrams (Fig. S4) allow us to identify which doped structures can form in equilibrium and which are compatible with stability of the corresponding pristine structure. For 1T, we find that the hollow adatom site is favored almost throughout the pristine stability region, although due to different reconstructions the 3×3 case also permits Mo- and S-substitution. The 1H diagram is similar to 2H, with a shift to higher chemical potentials, and the Mo-atop adatom site is favored in the pristine stability region. Finally, the 3R phase diagram closely resembles the 2H one,¹⁷ and only the Mo/S-atop intercalation is compatible with pristine stability, except at the highest doping levels. The other doping sites are predicted to be accessible only out of equilibrium.

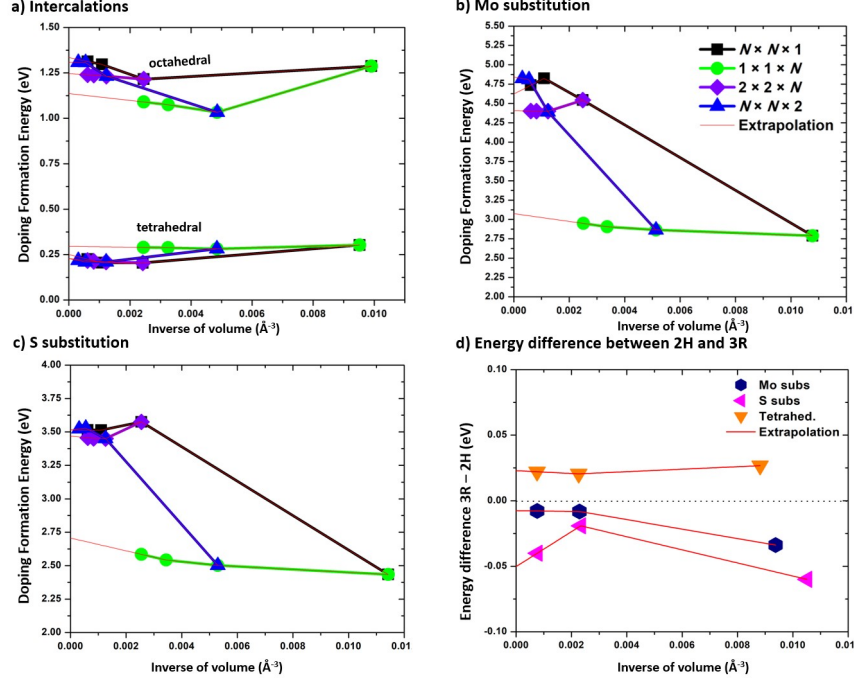


Figure 7: Doping formation energy in Ni-doped 2H-MoS₂ with respect to volume per Ni atom, in a) intercalations, b) Mo substitution (under Mo-rich conditions) and c) S substitution (under S-rich conditions). For S-rich conditions, every point on (b) is shifted down by 3.06 eV (making the lowest points slightly negative); for Mo-rich conditions, every point on (c) is shifted down by 1.53 eV. The doping formation energy is calculated with reference to bulk Ni, Mo, S and pristine 2H-MoS₂. N is the parameter for the supercell size. The supercell series varying along the z -axis do not change much in doping formation energy while series varying in xy plane change initially but then converge. Tetrahedral intercalation is favored over octahedral by a fairly constant amount at all supercells. Red lines show extrapolation to the low-doping limit. d) Energy difference per Ni atom between Ni-doped 2H and 3R structures with 24, 8, and 2 units of MoS₂ from left to right.

3.2 Structural parameters

Incorporating Ni into MoS₂ not only changes the energy, but also can cause local changes in structure, which we study through changes in bond lengths and lattice parameters. The maximum difference in Ni-S and Ni-Mo bond lengths with respect to the pristine Mo-S bond length is around 8% for the highest doping concentration (1 Ni in $1 \times 1 \times 1$ 2H-MoS₂) in substitution sites. Mo-S bond lengths away from the doping site were very close to the pristine Mo-S bond (differing by less than 0.04 Å), showing only a local effect on the structure. For the $1 \times 1 \times 1$ supercell of 2H, the Ni-S bond length in Mo substitution was 2.23

Å and the Ni-Mo bond in S substitution was 2.55 Å. The Mo-S bond length in pristine MoS₂ is 2.41 Å, so this is a reduction in the bond length in Mo substitution, and an elongation in S substitution, as shown in Table 1. Similarly, the bond lengths for substitutional doping in all 2H and 3R structures are consistent with a covalent bond, judging by the covalent radii⁴⁴ (Mo = 1.54 Å, Ni = 1.24 Å, S = 1.05 Å), which provide typical covalent bond lengths of 2.29 Å for Ni-S and 2.78 Å for Ni-Mo. Tetrahedral intercalation also shows covalent bonds: the Ni-Mo and Ni-S bond lengths are 2.73 Å and 2.15 Å respectively, which are far lower than the sum of Van der Waals radii (S=1.81 Å,⁴⁵ Ni=1.97 Å⁴⁶ and Mo=2.16 Å⁴⁶), clearly showing that intercalated Ni has covalent rather than Van der Waals interactions, in agreement with our previous results based on electron density.¹⁷ For comparison, the S-S distance between pristine MoS₂ layers is 3.59 Å which is close to the sum of the Van der Waals radii of two S atoms. For a concentration less than 1% of Mo substitution in both 2H and 3R, we found only 4 Ni-S bonds instead of 6, breaking the symmetry in a pseudo-Jahn-Teller distortion. A similar five-fold coordination was calculated¹² for Ni substituting Mo at a 2H basal plane surface, attributed to population of anti-bonding *d*-orbitals by extra charge from Ni. Four-fold coordination like our result was reported in a previous theoretical calculation for Mo-substituted 2H-MoS₂ in few-layer nanosheets.⁴⁷

Table 1: Bond length comparison in 2H and 3R with Mo and S substitution by Ni.

Pristine Mo-S=2.41 Å	2H (1 × 1 × 1)	2H (4 × 4 × 1)	3R (1 × 1 × 1)	3R (4 × 4 × 1)	Covalent radii sum
Ni-S (Mo subs)	2.23 Å	2.23 Å	2.25 Å	2.24 Å	2.29 Å
Ni-Mo (S subs)	2.67 Å	2.55 Å	2.58 Å	2.55 Å	2.78 Å

The 1H monolayer showed structural effects similar to the 2H phase. In Mo substitution, the Ni-S bond is decreased (compared to the pristine Mo-S bond of 2.41 Å) to 2.34 Å, and in S substitution the Ni-Mo bond is increased to 2.51 Å, for all supercells considered. Mo-atop has an Ni-Mo bond length of 2.55 Å and S-atop has an Ni-S bond length of 1.96 Å. As in bulk, the bond lengths are close to the sums of covalent radii except for the S-atop case, which is considerably shorter, presumably due to the fact that Ni is forming only one bond.

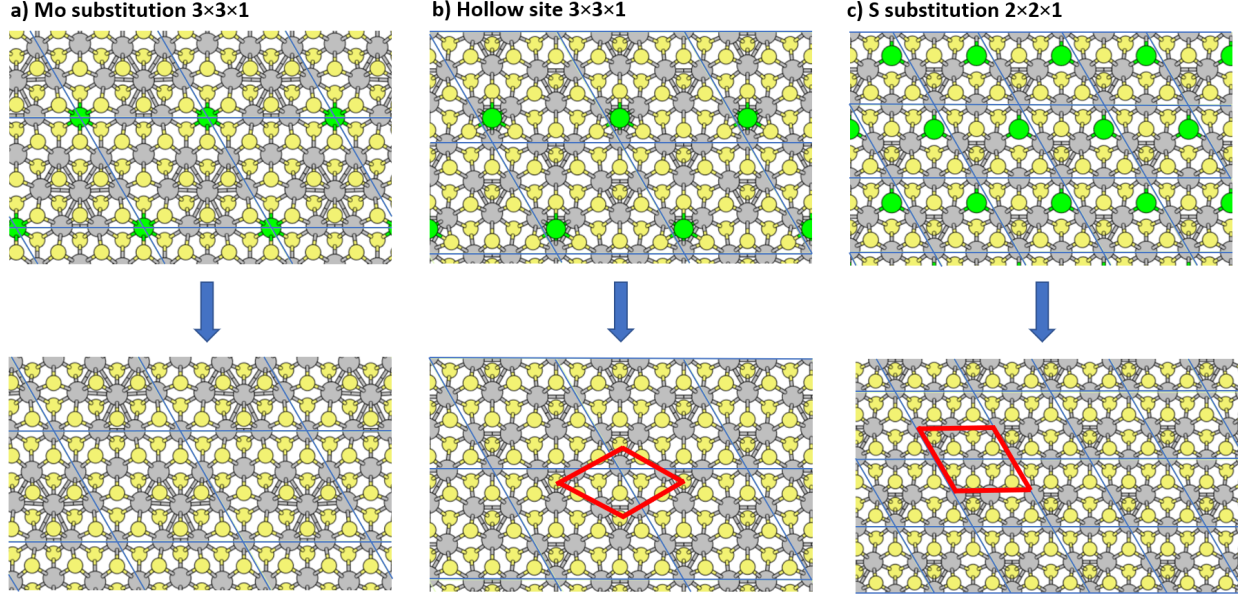


Figure 8: Reconstructed phases found in Ni-doped 1T with different Mo-Mo atom clustering. The upper row is the structure with Ni-doping (shown in green); the lower row is the structure after removal or replacement of Ni atom with appropriate Mo or S atom, and relaxation. The red diamond is the reconstructed primitive unit cell. Lattice parameters and reconstructions in lower row: (a) 9.73 Å, $3a \times 3a$ structure, which does not seem to have been previously reported; (b) 5.64 Å, $a\sqrt{3} \times a\sqrt{3}$ structure; and (c) 6.44 Å, $2a \times 2a$ structure, in accordance with Ref.⁴⁸

However, different kinds of distortions occur in the monolayer 1T phase related to its instability to 1T' and other reconstructions.^{35,48} Various patterns of Mo-atom clustering in the relaxed structures were observed depending on supercell size and doping scheme. To determine if the corresponding pristine structures were stable or would relax back to the original 1T phase, we returned the doped structures to pristine by removing adatoms or restoring Mo or S atoms to Ni-substituted sites, and relaxed the resulting structures. Most of the structures relaxed to previously known phases^{32,33,35,48} ($2a \times 2a$ or $a\sqrt{3} \times a\sqrt{3}$) while a few structures were not found in the literature and seem to be new metastable phases of 1T. Note that $N \times N$ supercells for even N are compatible with only $2a \times a$ or $2a \times 2a$ structures, while the 3×3 supercell is commensurate with $a\sqrt{3} \times a\sqrt{3}$. The details of new phases after removal/replacement with relaxation are shown in Table S7: the identified phases' lattice parameter and Mo-Mo distance are close to those of Zhuang *et al.*,⁴⁸ who calculated an

Mo-Mo distance of 2.77 Å for $2a \times 2a$ and 2.83 Å for $a\sqrt{3} \times a\sqrt{3}$ though we also have a lower-energy and less closely clustered $a\sqrt{3} \times a\sqrt{3}$ resulting from S substitution. Examples of Mo-Mo clustering with doping and after removal/replacement are shown in Fig. 8. The $2a \times 2a$ and $a\sqrt{3} \times a\sqrt{3}$ structures are 0.21 eV and 0.19 eV per MoS₂ lower in energy than 1T respectively. The phases not previously reported are obtained from $3 \times 3 \times 1$ and $4 \times 4 \times 1$ Mo substitution, and the energies are 0.08 eV and 0.15 eV per MoS₂, respectively: lower than 1T, but higher than the other reconstructions.

Turning our attention to the lattice parameters, the change in plane (a and b) was small (less than 2%) for all doping sites and polytypes (see Table 2). However, the c -parameter (out of plane) decreases slightly in the 2H and 3R phases in substitutional cases. In intercalations, the c -parameter was reduced slightly, though perhaps not significantly (within error bars). This is notable because intercalations are usually expected to increase the c -parameter due to Van der Waals interaction with the intercalant.^{30,49} However, as we previously showed, intercalated Ni forms covalent bonds,¹⁷ resulting in little or no change in interlayer spacing on intercalation. We present an error bar in c -parameters in Table 2 due to the insensitivity in total energy change in the c -direction with weak Van der Waals interactions (not observed along the stronger-bonded a - and b -directions). This error bar is calculated by parabolic fitting of the total energy per MoS₂ vs c and finding the range where the energy is within 0.01 eV of the minimum. Table 2 summarizes the overall effect in lattice parameters for $2 \times 2 \times 1$ supercells, which is a dopant concentration of 16% for substitution and 14% for intercalation in 2H. As we lower the doping concentration (for example in a $3 \times 3 \times 1$ supercell), lattice parameters necessarily converge towards the pristine value, as the effect of a single Ni atom is diluted among pristine surroundings.

We have also analyzed the vertical displacement of atoms in an Mo or S plane. Fig. 9 shows the planes of Mo atoms under Mo substitution by Ni in the 2H phase. The Mo plane containing Ni has an uneven surface where the maximum displacement of an Ni atom is 0.24 Å and the maximum displacement of an Mo atom is 0.10 Å with respect to the

pristine plane, occurring mostly for nearest neighbors of Ni. The planes of Mo and S in the unsubstituted sheet have negligible shifts and are smooth in all of the doped structures. The two S planes sandwiching the substituted Mo plane also have uneven surfaces: S atoms near to Ni were displaced up to 0.22 Å towards the Mo plane. In S substitution, only the Ni atom was significantly displaced, while the shift was negligible for all atoms in their respective planes. Intercalations showed smooth surfaces with negligible shifts of atoms with their respective planes. Such rough planes in Mo substitution could reduce the effective contact area, resulting in a lower coefficient of friction.

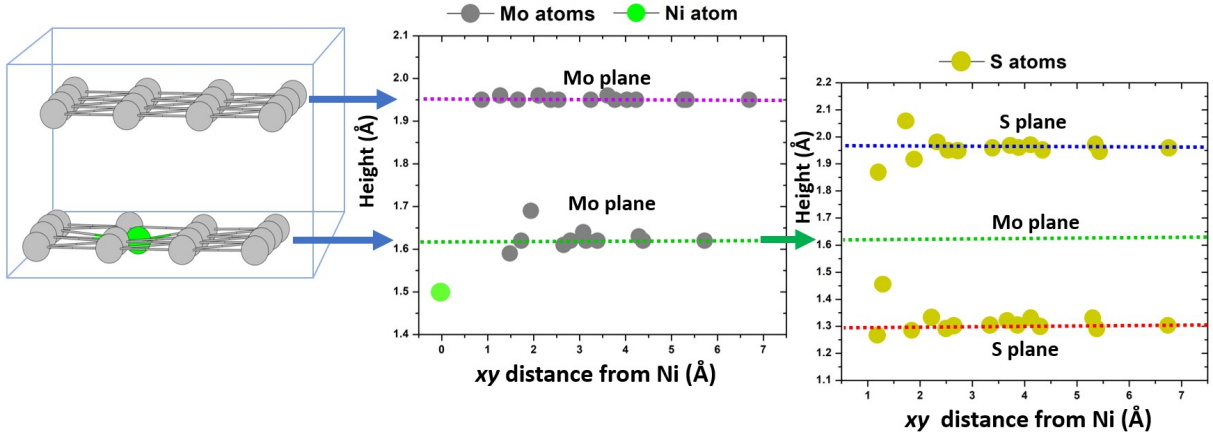


Figure 9: Vertical atomic displacements in Mo-substituted 2H phase, with planes shifted vertically to show changes clearly. Blue arrows point to the plotted heights of the Mo planes. Center: height of atoms with respect to pristine, indicated by green and purple dotted lines. Right: the two S-planes sandwiching the Mo-plane containing Ni. Most changes in height are observed close to the Ni-atom.

These structural results can be a guide to identifying the doping site in Ni-doped MoS₂. Small expansion or unaltered interlayer spacing, which can be detected by X-ray diffraction⁴³ or atomic force microscopy measurements,⁵⁰ indicates the presence of intercalants. The contraction of interlayer spacing indicates substitutional doping, consistent with recent experimental work on Ni-doped MoS₂: Mosconi *et al.*⁴³ found layer contraction in a sample believed to have Mo substitution. Thin films made under an excess of sulfur,⁵¹ which favors Mo substitution,¹⁷ were found to have a layer contraction increasing with Ni concentration, and also an increasing nanoscale roughness, consistent with our results. Lieber and Kim⁵⁰

Table 2: The lattice parameters a and c (all in Å) for different polytypes and doping cases, in a $2 \times 2 \times 1$ supercell. In all cases we found $a = b$. The lattice parameters are expressed in terms of the conventional unit cell of the pristine phases of MoS₂. The error bar for c comes from the insensitivity of the energy change along the c -direction, where the threshold is set to 0.01 eV. Only substitutional doping decreases the c -parameter whereas the intercalations lie mostly within the error bar of pristine and the mean values indicate little or no expansion along c . The monolayers do not have a c -parameter.

System	c (2H)	a (2H)	c (3R)	a (3R)	a (1H)	a (1T)
Pristine	12.4 ± 0.1	3.19	18.5 ± 0.1	3.19	3.19	3.18
Mo subs.	12.3 ± 0.1	3.20	18.4 ± 0.1	3.20	3.21	3.21
S subs.	12.2 ± 0.1	3.17	18.3 ± 0.1	3.18	3.15	3.16
Intercal./ adatom	12.5 ± 0.2 (tetrahed.)	3.19	18.7 ± 0.2 (Mo/S-atop tetrahed.)	3.20	3.20 (Mo-atop)	3.20 (Mo-atop)
Intercal./ adatom	12.4 ± 0.2 (octahed.)	3.19	18.5 ± 0.2 (trigon. pyram.)	3.19	3.19 (S-atop)	3.23 (hollow)

interpreted lack of change in the in-plane lattice in atomic force microscopy (AFM) measurements of Ni-doped MoS₂ as indicative of Mo substitution, but our results shows little change in a in any case. Instead, from our results, we propose that Mo or S substitution can be distinguished by observing contracted Ni-S bonds (Mo substitution) or elongated Mo-Ni bonds (S substitution) via transmission electron microscopy (TEM), scanning tunneling microscopy (STM), or extended X-ray absorption fine structure (EXAFS). Thus, these results may be useful to experimentalists to characterize the Ni location in MoS₂.

3.3 Electronic properties

We studied the electronic properties to understand the nature of bonding as well as to provide the effects of Ni-doping that may be useful for electronic applications. When undoped, the 1T phase is metallic, 1H is a direct-gap semiconductor, and 2H and 3R are indirect-gap semiconductors.^{52,53} The density of states for MoS₂ polytypes is shown in Fig. S9. We find that Mo substitution makes semiconducting bulk phases (2H and 3R) metallic, as shown in Fig. 10. The partial density of states (PDOS) calculation reveals that such metallic character arises due to contributions at the Fermi level from d orbitals of Mo and Ni and p orbitals from

S. S substitution and intercalations in 2H and 3R preserved the semiconducting gap. In the 1H monolayer, Mo substitution showed a single in-gap state whereas S substitution showed two in-gap states at the band edges as shown in Fig. 10(c)-(d). S-atop also has in-gap states and other adatoms in 1H are semiconducting as shown in Fig. S5. These in-gap states are due to d -orbitals of Mo and Ni and p -orbitals from S, as in 2H substitution. Zhao *et al.*²⁵ similarly reported two in-gap states at the band edges for S-substituted 1H. All the adatom cases in 1H showed semiconducting behavior. 1T, on the other hand, showed a metal-to-semiconductor transition in most cases we considered; only Mo-substituted $2 \times 2 \times 1$ and $3 \times 3 \times 1$, S-substituted $4 \times 4 \times 1$, Mo-atop $3 \times 3 \times 1$, and S-atop $2 \times 2 \times 1$ and $4 \times 4 \times 1$ remained metallic. This anomalous electronic behavior comes from the reconstructed clustering of Mo atoms which depends on both doping scheme and doping concentration. The gaps and density of states plots are given in Table S8 and Fig. S6-S8. Also, as discussed in Section 3.2, of the new phases in 1T after removal/replacement of Ni with relaxation, some are metallic and some semiconducting, as shown in Fig. S10-S11.

These results are relevant for possible applications: the in-gap states could be useful for optoelectronic applications such as quantum emitters.^{54,55} The metallic Mo-substituted 2H-MoS₂ could be used as an electrode for electrochemical energy storage devices, as semiconducting pristine 2H-MoS₂ is not an ideal electrode material⁵⁶ and attempts have been made to enhance electrical conductivity by forming hybrid electrodes.^{57,58} The metallic nature for 3R also suggests suitability of Ni substituting Mo as an active site for catalysis, as is well established for 2H.⁵⁹ The conductivity of Mo-substituted 2H- or 3R-MoS₂ could be identified by transport measurements or STM as a way of determining the doping site, in conjunction with the characteristic structural parameters mentioned in the previous section. Indeed, a recent study⁵¹ grew Ni-doped MoS₂ under S-rich conditions, which favors Mo substitution,¹⁷ and found decreasing resistivity with Ni concentration, consistent with our results.

The oxidation state of Ni, as measured by X-ray photoelectron spectroscopy (XPS), has

been used to infer the location of doping by transition metals¹⁶ in MoS₂. For example, XPS has found Ni⁰ and Ni²⁺ in Ni-doped 2H-MoS₂,⁶⁰ which could be assumed to represent intercalation and Mo substitution. While the relation between oxidation states and local charges in *ab initio* calculations is not simple, to investigate this issue, we first computed local charges on each atom by Löwdin charges⁶¹ (similar to an integration of the PDOS) and found only small changes in local electron numbers for Mo and S in doped MoS₂ compared to pristine. In 2H, Ni has the most partial positive charge in Mo substitution (+0.75 e), followed by intercalations (+0.52 e) and S substitution (+0.38 e) as least positive. We find only a small dependence on supercell sizes, and similar results for 1H as for 2H, which does not suggest detectable differences in XPS. On the other hand, we also tried the more advanced method of Sit *et al.*⁶² for assigning oxidation states based on *d*-orbital occupations from spin-polarized DFT+*U* calculations, using *U* values of 5.5 eV for Ni⁶³ and 4 eV for Mo.⁶⁴ We found an oxidation state of Ni⁴⁺ in Mo substitution at high Ni concentrations in 2H (>16%), 3R (>11%), and 1H (>8%), and all concentrations in 1T; lower concentrations showed Ni²⁺ in 1H, 2H, and 3R. S substitution and intercalations/adatoms showed Ni²⁻ in all polytypes. By contrast, the oxidation state for Mo in both pristine and doped systems could not be unambiguously assigned in this approach. These results indicate XPS can help detect Ni-doping sites, and are consistent with the idea of Ni²⁺ for Mo substitution, though we find the unusual Ni²⁻ for intercalation and adatoms instead of Ni⁰ which has been previously expected.

We also checked the presence of magnetic moments. While bulk Ni is ferromagnetic, the magnetism is itinerant, not localized on Ni, and therefore adding Ni dopants does not typically cause magnetism. All Ni-doped 2H and 3R are non-magnetic. Total magnetic moments per cell in Mo-substituted 1H were 3.99 μ_B for a $4 \times 4 \times 1$ supercell, in accordance with a previous calculation,⁶³ and 3.62 μ_B for a $3 \times 3 \times 1$ supercell. No other doped 1H cases showed magnetization. 1T reconstructions generally showed magnetization: $1 \times 1 \times 1$ S substitution and S-atop had 0.46 μ_B and 0.79 μ_B respectively, $2 \times 2 \times 1$ S substitution

had $0.22 \mu_B$, $3 \times 3 \times 1$ S-atop and Mo-atop had $0.19 \mu_B$ and $0.58 \mu_B$ respectively, and S-substituted $4 \times 4 \times 1$ had $0.76 \mu_B$. In some cases (S-atop $3 \times 3 \times 1$ and S-substitution $2 \times 2 \times 1$) we have semiconducting magnets, which could be interesting for application in spintronics.⁶⁵

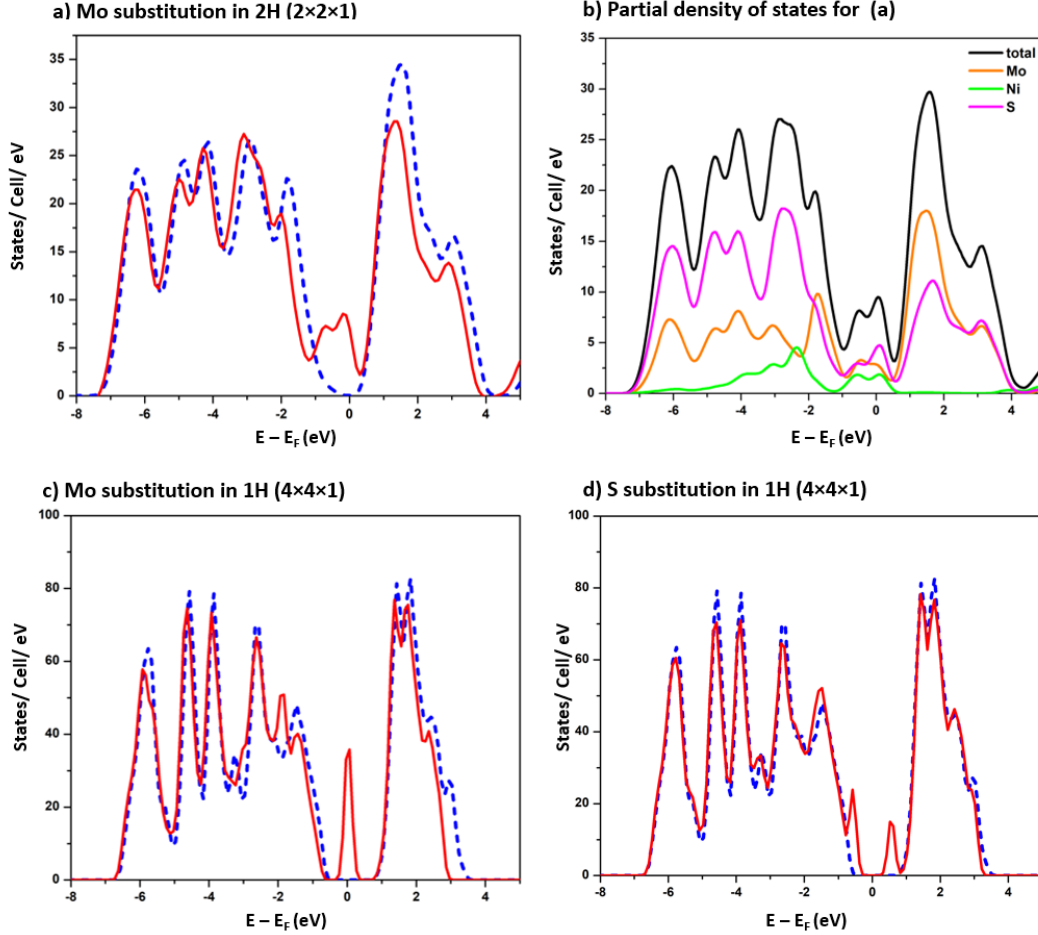


Figure 10: Density of states for doped 2H and 1H structures. The blue dotted curves in (a), (c), (d) are the pristine density of states. (b) shows the partial density of states for 2H with Mo substitution. Around the Fermi level, we find (a) metallic behavior, (c) one in-gap state, and (d) two in-gap states.

3.4 Layer dissociation energy

The layer dissociation energy is defined as the energy required to dissociate MoS₂ into separate layers and characterizes the binding strength between the layers, as used in the work

of Mounet *et al.*⁶⁶ to identify exfoliable and compounds from a large database. We use this concept to assess how MoS₂ layer binding changes with doping. We calculated the layer dissociation energy for pristine 2H- and 3R-MoS₂ as

$$\Delta E_{\text{pristine}} = NE_{1\text{H-pristine}} - E_{\text{bulk-pristine}} \quad (3)$$

where $\Delta E_{\text{pristine}}$ is the layer dissociation energy for pristine, N is the number of layers in a bulk system, $E_{1\text{H-pristine}}$ is the energy of the monolayer of equivalent size used in $E_{1\text{H-doped}}$, and $E_{\text{bulk-pristine}}$ is the energy of the undoped bulk system. Similarly, the layer dissociation energy for the doped system is given by:

$$\Delta E_{\text{doped}} = E_{1\text{H-doped}} + (N - 1)E_{1\text{H-pristine}} - E_{\text{bulk-doped}} \quad (4)$$

where $E_{1\text{H-doped}}$ is the energy of the doped monolayer of equivalent size and structure as used in $E_{1\text{H-pristine}}$, and $E_{\text{bulk-doped}}$ is the energy of the doped bulk system. To illustrate this, consider the $2 \times 2 \times 2$ supercell of 2H with Mo substitution by Ni. Here, $N = 4$, $E_{\text{bulk-pristine}}$ is the energy of $2 \times 2 \times 2$ undoped MoS₂ (Mo₁₆S₃₂), $E_{1\text{H-pristine}}$ is the energy of $2 \times 2 \times 1$ undoped 1H (Mo₄S₈), $E_{1\text{H-doped}}$ is the energy of Mo-substituted $2 \times 2 \times 1$ 1H (NiMo₃S₈), and $E_{\text{bulk-doped}}$ is the energy of Mo-substituted $2 \times 2 \times 2$ 2H (NiMo₁₅S₃₂). Given these quantities, we define a relative layer dissociation energy by $\Delta E_{\text{rel}} = \Delta E_{\text{doped}} - \Delta E_{\text{pristine}}$ which accounts for changes due to doping and is per Ni dopant atom since all our supercells contain just one Ni atom. The absolute value of the layer dissociation energy in a supercell can be much bigger than the pristine primitive cell's, and so it is more convenient to analyze this relative quantity.

In intercalation cases, we need to consider whether the dopant will remain in place or relax to a more favorable site, as shown in left side of Fig. 4. For example, 2H octahedral intercalation consists of two hollow sites with respect to the two layers, and when the layers are dissociated, the dopant may remain as before in the hollow of one layer (adiabatic case),

or may relax to the most favorable site, Mo-atop, depending on the thermal energy available to overcome any barrier. ΔE_{rel} is always smaller with monolayer relaxation than in the adiabatic case. In tetrahedral intercalation of 2H, Ni remaining on the layer with S-atop has higher ΔE_{rel} than remaining on the layer with Mo-atop since Mo-atop in monolayer is more strongly bound (Section 3.1.1): the energy difference between Mo-atop and S-atop in 1H is 1.68 eV and the average difference in ΔE_{rel} in tetrahedral intercalation for Mo-atop and S-atop is 1.70 eV. For comparison, our calculation shows the layer dissociation energy is 0.15 eV per MoS₂ unit in the layer (0.27 N m⁻¹), which is consistent with the result 0.22 N m⁻¹ from experiment,⁶⁷ and ~ 0.32 N m⁻¹ from a more accurate random-phase approximation calculation.⁶⁸ We have considered the different doping cases and found that nearly all increase the binding energy in both 2H and 3R, as shown in Fig. 11. We also considered higher Ni concentration, *i.e.* Ni between each layer, and found that ΔE_{rel} increased, even though doping formation energy per Ni is similar.

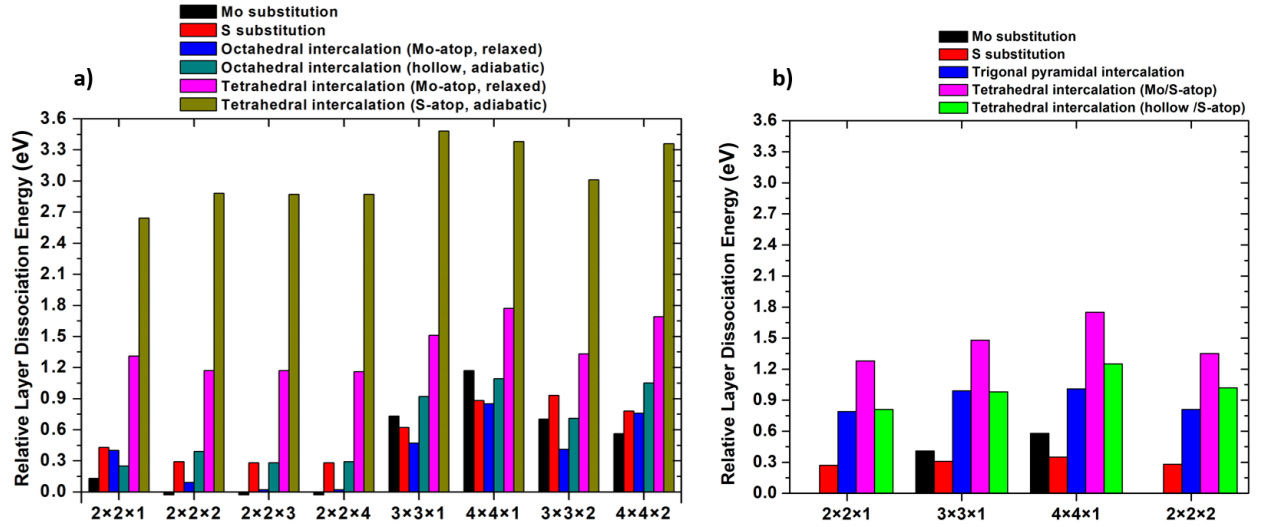


Figure 11: (a) Relative layer dissociation energy in 2H-MoS₂ for different doping sites and concentrations, showing a general increase in interlayer binding with doping. (b) Relative layer dissociation energy in 3R MoS₂. For 2H intercalations we consider both adiabatic and relaxed cases; for 3R intercalations we just use the relaxed (most stable) monolayers.

The additional binding between layers is strongest with intercalation while substitution has a lesser effect, consistent with Ni forming covalent bonds between layers.¹⁷ We note that

by contrast intercalation with other metals is found to *reduce* interaction between layers, as inferred from Raman spectroscopy for Li⁶⁹ and Ag.⁷⁰ In-plane supercell expansion generally increases ΔE_{rel} , suggesting bilayers will give similar results, whereas supercell expansion out of the plane has little effect. Ni-doping strengthens the binding between layers which can explain the experimental report of a reduced low wear rate in Ni-doped MoS₂²⁹ compared to pristine. The lower wear rate is an important parameter leading to longer life of MoS₂ material for lubrication application.²⁶ We may expect a similar trend in a related quantity, the work of adhesion, which is defined as the energy needed to divide the material in two, whereas the layer dissociation energy involves splitting apart all the layers. Pastewka *et al.*⁷¹ have argued that a larger work of adhesion increases contact area, which would be expected to increase the coefficient of friction, though this may be offset by the increase in atomistic roughness in doped layers.

Comparing tetrahedral intercalation (the most favorable structure for 2H and 3R), we see 3R has a higher layer dissociation energy in most cases, by 0.04 eV on average. The two structures have similar structural changes around Ni and a similar trend in doping formation energy. The doping formation energy and total energy have only a small difference between 2H and 3R tetrahedral intercalation: 2H is favored by 0.020 eV in doping formation energy and 0.022 eV in total energy. Insofar as the layer dissociation energy is determining the wear rate, we do not expect significant differences in wear between these two phases. Layer sliding simulations for bilayer MoS₂ in 2H and 3R-type configurations found that under load 3R has the less corrugated sliding path, both spatially and energetically, suggesting better lubricant properties.⁷² Based on this, Ni-doped 3R may be an attractive target for further lubrication studies, with experimental tests of coefficient of friction and wear.

4 Conclusion

In this work, we studied MoS₂ and its different phases by doping with Ni. First, we found that the most energetically favorable sites for Ni-doping are adatom on Mo (Mo-atop) in 1H monolayer, adatom in hollow in 1T monolayer, tetrahedral intercalation in 2H bulk and 2H like intercalation in 3R (Mo/S-atop). In bulk phases, irrespective of doping concentration, we found Ni bond length contraction for Mo substitution and expansion in S substitution, *vs.* Mo-S bonds. The bulk lattice parameter out of plane contracted at high concentration of substitutional Ni but was unaltered or expanded for intercalation, which can serve as experimental signatures of substitution *vs* intercalation. The Mo-S bond lengths away from the dopant were close to pristine, and lattice parameters converged to pristine at lower doping concentration indicating that Ni-doping has only a local effect. On the other hand, we also found the possibility of phase change from 2H to 3R with Mo or S substitution, and the Ni-doped 1T phase formed reconstructed phases, based on the pristine structures such as $2a \times 2a$ or $a\sqrt{3} \times a\sqrt{3}$. While most doped structures were semiconducting, we found that semiconducting 2H and 3R became metallic with Mo substitution by Ni, of interest for electrochemical or catalytic applications, whereas Mo or S substitution in 1H was semiconducting with in-gap states of potential interest for quantum emitters. Ni-doping of 1T mostly showed metal-to-semiconductor transitions due to the reconstructions, and typically caused a small magnetic moment. We find oxidation states characteristic of doping site, which can be probed by XPS: Mo substitution has Ni⁴⁺ or Ni²⁺, and S substitution, intercalations and adatoms have Ni²⁻, for all polytypes. Lastly, we computed the layer dissociation energy where doped MoS₂ shows stronger binding between layers than pristine, particularly for intercalations – in contrast to findings for other transition metals. In conclusion we present local effects on bonding and structural changes, a possibility of phase change, interesting electronic properties upon Ni-doping and finally strongly increased interlayer interactions. This layer dissociation energy relates to improved lubrication performance lifetime (wear) for doped MoS₂. Our results suggest that the Ni-doped 3R polytype may not have significant

differences in wear rate than 2H and we propose further exploration of the friction properties of 3R, along with investigation of potential electronic and optical applications of Ni-doped MoS₂.

Methods

Our calculations use plane-wave density functional theory (DFT) implemented in the code Quantum ESPRESSO, version 6.1.^{73,74} We used the Perdew-Burke-Ernzerhof (PBE) generalized gradient approximation⁷⁵ for all of our analysis except for the doping formation energy which is calculated with Perdew-Wang⁷⁶ local density approximation (LDA) functional. With PBE, we used the semi-empirical Grimme-D2 (GD2)⁷⁷ Van der Waals correction to the total energy, which gives lattice parameters and other properties considerably closer to experimental results for MoS₂, as demonstrated by other researchers.^{17,78} Calculation with LDA has also been shown to give accurate lattice parameters.¹⁷ The doping formation energy requires the energies of metal solids such as Ni and Mo which are not well described by PBE+GD2,⁷⁹ and therefore we used LDA for these calculations to obtain accurate energies for both metals and doped MoS₂ as in our previous work on 2H-MoS₂.¹⁷ We used Optimized Norm-Conserving Vanderbilt pseudopotentials⁸⁰ parametrized by Schlipf and Gygi⁸¹ from the SG15 set⁸² generally, except we used the Pseudodojo⁸³ set for partial density of states (PDOS), to have available pseudo-wavefunctions; and for LDA, to be consistent with our previous calculations.¹⁷ Kinetic energy cutoffs of 816 eV (60 Ry) for PBE and 1088 eV (80 Ry) for LDA were used. Half-shifted k -point grids of $6 \times 6 \times 2$ for bulk and $12 \times 12 \times 1$ for monolayers (in the pristine case) were chosen to converge the total energies within 0.001 eV/atom. Atomic coordinates were relaxed using a force threshold of 1.0×10^{-4} Ry/bohr and the stresses were relaxed below 0.1 kbar. We used a Gaussian smearing of 0.05 eV for the bulk metals or whenever metallic cases arose. For doped structures, we decreased the k -grid in x -, y - or z -directions in proportion to the supercell size, to maintain consistent

Brillouin zone sampling. For density of states calculations, a broadening of 0.02 eV and k -grid sampling of $20 \times 20 \times 1$ for $4 \times 4 \times 1$ monolayers and $20 \times 20 \times 10$ for $2 \times 2 \times 1$ bulk was used.

The doping concentration is varied by putting a single Ni atom in increasing supercells such as $2 \times 2 \times 1$, $3 \times 3 \times 1$, $3 \times 3 \times 2$, etc. In the 2H structure, we also considered tetrahedrally intercalated structures with two Ni atoms per cell, one between each pair of layers, vertically above one another. Our supercells represent not only approximations to a disordered low-doping limit, but also possible ordered phases, as are found for Li intercalation.³⁰ The Ni atom fraction ranges from a minimum of 0.5% to maximum of 17%. The monolayers contain vacuum of 15 Å between layers to reduce the effect of spurious periodicity. We have tested the monolayers with dipole corrections⁸⁴ in case there would be an out-of-plane dipole moment in the doped phases, but the change in total energy was negligible ($\sim 10^{-4}$ eV) and structural parameters were unaffected. Our calculations in general are non-spin-polarized, as use of spin polarization did not significantly change the energy (less than 0.1 meV per atom). However, we used spin-polarized calculations for ferromagnetic bulk Ni, and also for test calculations on each doping case to check for magnetic moments.

Before calculations on doped systems, the structure of 2H-MoS₂ was bench-marked with PBE+GD2 and lattice parameters were calculated as $a = b = 3.19 \pm 0.02$ Å and $c = 12.4 \pm 0.2$ Å. The uncertainties come from a cubic fit to the total energy as a function of the lattice parameters. These results are in good agreement with previous theoretical and experimental calculations.^{52,85} For the energies of reference elemental phases, bulk Mo and Ni are calculated in body-centered and face-centered cubic lattice of 3.19 Å and 3.52 Å, respectively, with a $12 \times 12 \times 12$ half-shifted k -grid. For bulk S, a unit cell containing 48 atoms⁸⁶ is calculated with a $3 \times 3 \times 3$ k -grid. The energies of these reference phases, as in our previous work,¹⁷ are used to calculate the doping formation energy.

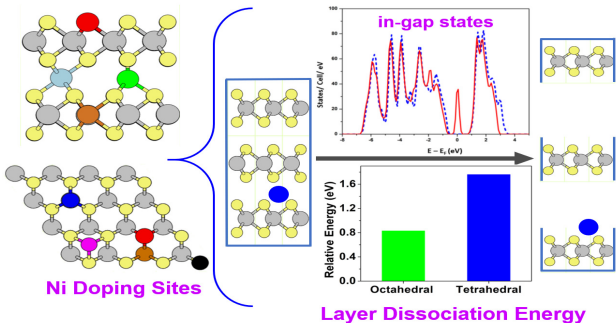
Data Availability

The datasets generated during and/or analysed during the current study are available from the corresponding author on reasonable request.

Supplementary Information

Doping formation energy tables, density of states for Ni-doped and pristine polytypes (PDF). `structures.tar.gz` file contains relaxed atomic coordinates for Ni-doped MoS₂ polytypes, pristine polytypes, 1T reconstructed structures and 3R primitive unit cell (XSF).

Table of Contents Image



Acknowledgments

We acknowledge useful discussions with Ashlie Martini and Mehmet Baykara. This work was supported by UC Merced start-up funds and the Merced nAnomaterials Center for Energy and Sensing (MACES), a NASA-funded research and education center, under award NNX15AQ01. This work used computational resources from the Multi-Environment Computer for Exploration and Discovery (MERCED) cluster at UC Merced, funded by National Science Foundation Grant No. ACI-1429783, and the National Energy Research Scientific Computing Center (NERSC), a U.S. Department of Energy Office of Science User

Author Contributions

R.K. and E.G. performed calculations, R.K. and D.A.S. wrote the manuscript, and D.A.S. supervised the project.

Competing Interests

The authors declare no competing interests.

References

- (1) Splendiani, A.; Sun, L.; Zhang, Y.; Li, T.; Kim, J.; Chim, C.-Y.; Galli, G.; Wang, F. Emerging Photoluminescence in Monolayer MoS₂. *Nano Lett.* **2010**, *10*, 1271–1275.
- (2) Mak, K. F.; Lee, C.; Hone, J.; Shan, J.; Heinz, T. F. Atomically Thin MoS₂: A New Direct-Gap Semiconductor. *Phys. Rev. Lett.* **2010**, *105*, 136805.
- (3) Li, Y.; Zhou, Z.; Zhang, S.; Chen, Z. MoS₂ Nanoribbons: High Stability and Unusual Electronic and Magnetic Properties. *J. Am. Chem. Soc.* **2008**, *130*, 16739–16744.
- (4) Kaasbjerg, K.; Thygesen, K. S.; Jacobsen, K. W. Phonon-limited mobility in n-type single-layer MoS₂ from first principles. *Phys. Rev. B* **2012**, *85*, 115317.
- (5) Lin, Z.; Carvalho, B. R.; Kahn, E.; Lv, R.; Rao, R.; Terrones, H.; Pimenta, M. A.; Terrones, M. Defect engineering of two-dimensional transition metal dichalcogenides. *2D Mater.* **2016**, *3*, 022002.
- (6) Lembke, D.; Kis, A. Breakdown of High-Performance Monolayer MoS₂ Transistors. *ACS Nano* **2012**, *6*, 10070–10075.

- (7) Mao, J.; Wang, Y.; Zheng, Z.; Deng, D. The rise of two-dimensional MoS₂ for catalysis. *Front. Phys.* **2018**, *13*, 138118.
- (8) Radisavljevic, B.; Radenovic, A.; Brivio, J.; Giacometti, V.; Kis, A. Single-layer MoS₂ transistors. *Nat. Nanotech.* **2011**, *6*, 147–150.
- (9) Lopez-Sanchez, O.; Lembke, D.; Kayci, M.; Radenovic, A.; Kis, A. Ultrasensitive photodetectors based on monolayer MoS₂. *Nat. Nanotech.* **2013**, *8*.
- (10) Krause, O. et al. High-precision cryogenic wheel mechanisms of the JWST/MIRI instrument: performance of the flight models. *SPIE* **2010**, *7739*, 421 – 432.
- (11) Jeong, G.; Kim, C. H.; Hur, Y. G.; Han, G.-H.; Lee, S. H.; Lee, K.-Y. Ni-Doped MoS₂ Nanoparticles Prepared via Core–Shell Nanoclusters and Catalytic Activity for Upgrading Heavy Oil. *Energy Fuels* **2018**, *32*, 9263–9270.
- (12) Hakala, M.; Kronberg, R.; Laasonen, K. Hydrogen adsorption on doped MoS₂ nanostructures. *Sci. Rep.* **2017**, *7*, 15243.
- (13) Ma, X.; Li, J.; An, C.; Feng, J.; Chi, Y.; Liu, J.; Zhang, J.; Sun, Y. Ultrathin Co(Ni)-doped MoS₂ nanosheets as catalytic promoters enabling efficient solar hydrogen production. *Nano Res.* **2016**, *9*, 2284–2293.
- (14) Jun-Feng, Y.; Braham, P.; Qian-Feng, F. Tribological properties of transition metal di-chalcogenide based lubricant coatings. *Front. Mater. Sci.* **2012**, *6*, 116–127.
- (15) Ma, D.; Ju, W.; Li, T.; Zhang, X.; He, C.; Ma, B.; Lu, Z.; Yang, Z. The adsorption of CO and NO on the MoS₂ monolayer doped with Au, Pt, Pd, or Ni: A first-principles study. *Appl. Surf. Sci.* **2016**, *383*, 98 – 105.
- (16) Tedstone, A. A.; Lewis, D. J.; O’Brien, P. Synthesis, Properties, and Applications of Transition Metal-Doped Layered Transition Metal Dichalcogenides. *Chem. Mater.* **2016**, *28*, 1965–1974.

- (17) Guerrero, E.; Karkee, R.; Strubbe, D. A. Phase stability and Raman/IR signatures of Ni-doped MoS₂ from DFT studies. **2020**, <https://arxiv.org/abs/2010.02198>.
- (18) Savage, R. H. Graphite Lubrication. *J. Appl. Phys.* **1948**, *19*, 1.
- (19) Khare, H. S.; Burris, D. L. The Effects of Environmental Water and Oxygen on the Temperature-Dependent Friction of Sputtered Molybdenum Disulfide. *Tribology Lett.* **2013**, *52*, 485–493.
- (20) Lince, J. R. Effective Application of Solid Lubricants in Spacecraft Mechanisms. *Lubricants* **2020**, *8*, 74.
- (21) Stupp, B. Synergistic effects of metals co-sputtered with MoS₂. *Thin Solid Films* **1981**, *84*, 256–257.
- (22) Pope, L.; Jervis, T.; Nastasi, M. Effects of laser processing and doping on the lubrication and chemical properties of thin MoS₂ films. *Surf. Coat. Technol.* **1990**, *42*, 217 – 225.
- (23) Wells, R. C. Relative Abundance of Nickel in the Earth’s Crust. *U.S. Dept. of the Interior Professional Paper 205-A* **1943**, 1–21, <https://pubs.usgs.gov/pp/0205a/report.pdf>.
- (24) Schulz, K. J.; Piatak, N. M.; Papp, J. F. Niobium and Tantalum, chap. M of Schulz, K.J., DeYoung, J.H., Jr., Seal, R.R., II, and Bradley, D.C., eds., Critical mineral resources of the United States—Economic and environmental geology and prospects for future supply. *U.S. Geological Survey Professional Paper 1802* **2017**, M1–M34, <https://doi.org/10.3133/pp1802M>.
- (25) Zhao, B.; Liu, L.; Cheng, G.; Li, T.; Qi, N.; Chen, Z.; Tang, Z. Interaction of O₂ with monolayer MoS₂: Effect of doping and hydrogenation. *Mater. Des.* **2017**, *383*, 1 – 8.
- (26) Vazirisereshk, M. R.; Martini, A.; Strubbe, D. A.; Baykara, M. Z. Solid Lubrication with MoS₂: A Review. *Lubricants* **2019**, *7*, 57.

- (27) Renevier, N.; Fox, V.; Teer, D.; Hampshire, J. Coating characteristics and tribological properties of sputter-deposited MoS₂/metal composite coatings deposited by closed field unbalanced magnetron sputter ion plating. *Surf. Coat. Technol.* **2012**, *127*, 24–37.
- (28) Teer, D. New solid lubricant coatings. *Wear* **2001**, *251*, 1068–1074.
- (29) Vellore, A.; Garcia, S. R.; Johnson, D.; Martini, A. Ni-doped MoS₂ Dry Film Lubricant Life. *Adv. Mater. Interfaces* **2020**, *2001109*.
- (30) Benavente, E.; Santa-Ana, M.; Mendizábal, F.; González, G. Intercalation chemistry of molybdenum disulfide. *Coord. Chem. Rev.* **2002**, *224*, 87 – 109.
- (31) Suh, J. et al. Reconfiguring crystal and electronic structures of MoS₂ by substitutional doping. *Nat. Commun.* **2018**, *9*, 199.
- (32) Zhao, W.; Pan, J.; Fang, Y.; Che, X.; Wang, D.; Bu, K.; Huang, F. Metastable MoS₂: Crystal Structure, Electronic Band Structure, Synthetic Approach and Intriguing Physical Properties. *Chem. Eur. J.* **2018**, *24*, 15942–15954.
- (33) Ge, Y.; Wan, W.; Ren, Y.; Liu, Y. Large thermoelectric power factor of high-mobility transition-metal dichalcogenides with 1T'' phase. *Phys. Rev. Res.* **2020**, *2*, 013134.
- (34) Luo, R.; Luo, M.; Wang, Z.; Liu, P.; Song, S.; Wang, X.; Chen, M. The atomic origin of nickel-doping-induced catalytic enhancement in MoS₂ for electrochemical hydrogen production. *Nanoscale* **2019**, *11*, 7123.
- (35) Pal, B.; Singh, A.; G., S.; Mahale, P.; Kumar, A.; Thirupathaiah, S.; Sezen, H.; Amati, M.; Gregoratti, L.; Waghmare, U. V.; Sarma, D. D. Chemically exfoliated MoS₂ layers: Spectroscopic evidence for the semiconducting nature of the dominant trigonal metastable phase. *Phys. Rev. B* **2017**, *96*, 195426.
- (36) Qian, X.; Liu, J.; Fu, L.; Li, J. Quantum spin Hall effect in two-dimensional transition metal dichalcogenides. *Science* **2014**, *346*, 1344–1347.

- (37) XiaoBo, C.; ZhenLian, C.; Jun, L. Critical electronic structures controlling phase transitions induced by lithium ion intercalation in molybdenum disulphide. *Chin. Sci. Bull.* **2013**, *58*, 1632–1641.
- (38) Ivanovskaya, V. V.; Zobelli, A.; Gloter, A.; Brun, N.; Serin, V.; Colliex, C. Ab initio study of bilateral doping within the MoS₂-NbS₂ system. *Phys. Rev. B* **2008**, *78*, 134104.
- (39) Dolui, K.; Rungger, I.; Pemmaraju, C. D.; Sanvito, S. Possible doping strategies for MoS₂ monolayers: An ab initio study. *Phys. Rev. B* **2013**, *88*, 075420.
- (40) Zhao, C.; Jin, C.; Wu, J.; Ji, W. Magnetism in molybdenum disulphide monolayer with sulfur substituted by 3d transition metals. *J. Appl. Phys.* **2016**, *120*, 144305.
- (41) Hao, Y.; Wang, Y. T.; Xu, L. C.; Yang, Z.; Liu, R. P.; Li, X. Y. 1T-MoS₂ monolayer doped with isolated Ni atoms as highly active hydrogen evolution catalysts: A density functional study. *Appl. Surf. Sci.* **2019**, *469*, 292 – 297.
- (42) Makov, G.; Payne, M. C. Periodic boundary conditions in ab initio calculations. *Phys. Rev. B* **1995**, *51*, 4014–4022.
- (43) Mosconi, D.; Till, P.; Calvillo, L.; Kosmala, T.; Garoli, D.; Debellis, D.; Martucci, A.; Agnoli, S.; Granozzi, G. Effect of Ni Doping on the MoS₂ Structure and Its Hydrogen Evolution Activity in Acid and Alkaline Electrolytes. *Surfaces* **2019**, *2*, 531–545.
- (44) Cordero, B.; Gómez, V.; Platero-Prats, A. E.; Revés, M.; Echeverría, J.; Cremades, E.; Barragán, F.; Alvarez, S. Covalent radii revisited. *Dalton Trans.* **2008**, *21*, 2832–2838.
- (45) Aquilanti, V.; Ascenzi, D.; Braca, E.; Cappelletti, D.; Pirani, F. Production, characterization and scattering of a sulfur atom beam : Interatomic potentials for the rare-gas sulfides, RS (R = Ne, Ar, Kr, Xe). *Phys. Chem. Chem. Phys.* **2000**, *2*, 4081–4088.
- (46) Batsanov, S. Intramolecular Contact Radii Close to the van der Waals Radii. *Zh. Neorg. Khim.* **2000**, *45*, 992–996.

- (47) Deng, J.; Li, H.; Xiao, J.; Tu, Y.; Deng, D.; Yang, H.; Tian, H.; Li, J.; Rena, P.; Bao, X. Triggering the electrocatalytic hydrogen evolution activity of the inert two-dimensional MoS₂ surface via single-atom metal doping. *Energy Environ. Sci.* **2015**, *8*, 1594.
- (48) Zhuang, H. L.; Johannes, M. D.; Singh, A. K.; Hennig, R. G. Doping-controlled phase transitions in single-layer MoS₂. *Phys. Rev. B* **2017**, *96*, 165305.
- (49) Xie, J.; Zhang, J.; Li, S.; Grote, F.; Zhang, X.; Zhang, H.; Wang, R.; Lei, Y.; Pan, B.; Xie, Y. Controllable Disorder Engineering in Oxygen-Incorporated MoS₂ Ultrathin Nanosheets for Efficient Hydrogen Evolution. *J. Am. Chem. Soc.* **2013**, *135*, 17881–17888.
- (50) Lieber, C. M.; Kim, Y. Characterization of the structural, electronic and tribological properties of metal dichalcogenides by scanning probe microscopies. *Thin Solid Films* **1991**, *206*, 355–359.
- (51) Giang, H.; Adil, O.; Suni, I. I. Electrodeposition of Ni-doped MoS₂ Thin Films. *J. Electrochem. Soc.* **2020**, *167*, 082512.
- (52) Komsa, H.-P.; Krasheninnikov, A. V. Native defects in bulk and monolayer MoS₂ from first principles. *Phys. Rev. B* **2015**, *91*, 125304.
- (53) Coutinho, S.; Tavares, M.; Barboza, C.; Frazão, N.; Moreira, E.; Azevedo, D. L. 3R and 2H polytypes of MoS₂: DFT and DFPT calculations of structural, optoelectronic, vibrational and thermodynamic properties. *J. Phys. Chem. Solids* **2017**, *111*, 25 – 33.
- (54) Peyskens, F.; Chakraborty, C.; Muneeb, M.; Thourhout, D. V.; Englund, D. Integration of single photon emitters in 2D layered materials with a silicon nitride photonic chip. *Nat. Commun.* **2019**, *10*, 4435.
- (55) Schuler, B.; Qiu, D. Y.; Refaely-Abramson, S.; Kastl, C.; Chen, C. T.; Barja, S.; Koch, R. J.; Ogletree, D. F.; Aloni, S.; Schwartzberg, A. M.; Neaton, J. B.; Louie, S. G.;

- Weber-Bargioni, A. Large Spin-Orbit Splitting of Deep In-Gap Defect States of Engineered Sulfur Vacancies in Monolayer WS₂. *Phys. Rev. Lett.* **2019**, *123*, 076801.
- (56) Acerce, M.; Voiry, D.; Chhowalla, M. Metallic 1T phase MoS₂ nanosheets as supercapacitor electrode materials. *Nat. Nanotech.* **2015**, *10*, 313–318.
- (57) da Silveira Firmiano, E. G.; Rabelo, A. C.; Dalmaschio, C. J.; Pinheiro, A. N.; Pereira, E. C.; Schreiner, W. H.; Leite, E. R. Supercapacitor Electrodes Obtained by Directly Bonding 2D MoS₂ on Reduced Graphene Oxide. *Adv. Energy Mater.* **2014**, *4*, 1301380.
- (58) Huang, K.-J.; Wang, L.; Liu, Y.-J.; Wang, H.-B.; Liu, Y.-M.; Wang, L.-L. Synthesis of polyaniline/2-dimensional graphene analog MoS₂ composites for high-performance supercapacitor. *Electrochim. Acta* **2013**, *109*, 587–594.
- (59) Gómez-Balderas, R.; Martínez-Magadán, J. M.; Santamaria, R.; Amador, C. Promotional effect of Co or Ni impurity in the catalytic activity of MoS₂: An electronic structure study. *Int. J. Quantum Chem.* **2000**, *80*, 406–415.
- (60) Kondekar, N.; Boebinger, M. G.; Tian, M.; Kirmani, M. H.; McDowell, M. T. The Effect of Nickel on MoS₂ Growth Revealed with *in Situ* Transmission Electron Microscopy. *ACS Nano* **2019**, *13*, 7117–7126.
- (61) Löwdin, P. On the Non-Orthogonality Problem Connected with the Use of Atomic Wave Functions in the Theory of Molecules and Crystals. *J. Chem. Phys.* **1950**, *18*, 365.
- (62) Sit, P. H.-L.; Car, R.; Cohen, M. H.; Selloni, A. Simple, Unambiguous Theoretical Approach to Oxidation State Determination via First-Principles Calculations. *Inorg. Chem.* **2011**, *50*, 10259–10267.

- (63) Zhu, Y.; Liang, X.; Qin, J.; Deng, L.; Bi, L. Strain tunable magnetic properties of 3d transition-metal ion doped monolayer MoS₂: A first-principles study. *Int. J. Quantum Chem.* **2018**, *8*, 055917.
- (64) Wu, M.; Yao, X.; Hao, Y.; Dong, H.; Cheng, Y.; Liu, H.; Lu, F.; Wang, W.; Cho, K.; Wang, W.-H. Electronic structures, magnetic properties and band alignments of 3d transition metal atoms doped monolayer MoS₂. *Phys. Lett. A* **2018**, *382*, 111–115.
- (65) Liu, W.; Zhang, H.; Shi, J.; Wang, Z.; Song, C.; Wang, X.; Lu, S.; Zhou, X.; Gu, L.; Louzguine-Luzgin, D. V.; Chen, M.; Yao, K.; Chen, N. A room-temperature magnetic semiconductor from a ferromagnetic metallic glass. *Nat. Commun.* **2016**, *7*, 13497.
- (66) Mounet, N.; Gibertini, M.; Schwaller, P.; Campi, D.; Merkys, A.; Marrazzo, A.; Sohier, T.; Castelli, I. E.; Cepellotti, A.; Pizzi, G.; Marzari, N. Two-dimensional materials from high-throughput computational exfoliation of experimentally known compounds. *Nat. Nanotech.* **2018**, *13*, 246–252.
- (67) Tang, D.-M.; Kvashnin, D. G.; Najmaei, S.; Bando, Y.; Kimoto, K.; Koskinen, P.; Ajayan, P. M.; Yakobson, B. I.; Sorokin, P. B.; Lou, J.; Golberg, D. Nanomechanical cleavage of molybdenum disulphide atomic layers. *Nat. Commun.* **2014**, *4*, 3631.
- (68) Björkman, T.; Gulans, A.; Krasheninnikov, A. V.; Nieminen, R. M. Van der Waals Bonding in Layered Compounds from Advanced Density-Functional First-Principles Calculations. *Phys. Rev. Lett.* **2012**, *108*, 235502.
- (69) Sekine, T.; C., J.; Samaras, I.; Jouanne, M.; Balkanski, M. Vibrational Modifications on Lithium Intercalation in MoS₂. *Mat. Sci. Eng. B* **1989**, *3*, 153–158.
- (70) Sheremetyeva, N.; Niedzielski, D.; Tristant, D.; Liang, L.; Kerstetter, L. E.; Mohny, S. E.; Meunier, V. Low-frequency Raman signature of Ag-intercalated few-layer MoS₂. *2D Mater.* **2021**, *8*, 025031.

- (71) Pastewka, L.; Robbins, M. O. Contact between rough surfaces and a criterion for macroscopic adhesion. *Proc. Nat. Acad. Sci.* **2014**, *111*, 3298–3303.
- (72) Levita, G.; Cavaleiro, A.; Molinari, E.; Polcar, T.; Righi, M. C. Sliding Properties of MoS₂ Layers: Load and Interlayer Orientation Effects. *J. Phys. Chem. C* **2014**, *118*, 13809–13816.
- (73) Giannozzi, P. et al. QUANTUM ESPRESSO: a modular and open-source software project for quantum simulations of materials. *J. Phys.: Condens. Matt.* **2009**, *21*.
- (74) Giannozzi, P. et al. Advanced capabilities for materials modelling with Quantum ESPRESSO. *J. Phys.: Condens. Matt.* **2017**, *29*, 465901.
- (75) Perdew, J. P.; Burke, K.; Ernzerhof, M. Generalized Gradient Approximation Made Simple. *Phys. Rev. Lett.* **1996**, *77*, 3865–3868.
- (76) Perdew, J. P.; Wang, Y. Accurate and simple analytic representation of the electron–gas correlation energy. *J. Phys. Chem. C* **1992**, *45*, 13244.
- (77) Grimme, S. Semiempirical GGA-Type Density Functional Constructed with a Long-Range Dispersion Correction. *J. Comput. Chem.* **2006**, *27*, 1787–1799.
- (78) Peelaers, H.; de Walle, C. G. V. Elastic Constants and Pressure-Induced Effects in MoS₂. *J. Phys. Chem. C* **2014**, *118*, 12073–12076.
- (79) Andersson, M. P. Density Functional Theory with Modified Dispersion Correction for Metals Applied to Self-Assembled Monolayers of Thiols on Au(111). *J. Theor. Chem.* **2013**, *2013*, 2356–7686.
- (80) Hamann, D. R. Optimized norm-conserving Vanderbilt pseudopotentials. *Phys. Rev. B* **2013**, *88*, 085117.
- (81) Schlipf, M.; Gygi, F. Optimization algorithm for the generation of ONCV pseudopotentials. *Comp. Phys. Commun.* **2015**, *196*, 36–44.

- (82) *web* <http://www.quantum-simulation.org/potentials>,
- (83) *web* <http://www.pseudo-dojo.org>,
- (84) Bengtsson, L. Dipole correction for surface supercell calculations. *Phys. Rev. B* **1999**, *59*, 12301–12304.
- (85) McKeehan, L. W. The Crystal Structure of Iron-Nickel Alloys. *Phys. Rev.* **1923**, *21*, 402.
- (86) *web* <https://materialsproject.org/materials/mp-557869/>,